

Combining the band-limited parameterization and Semi-Lagrangian Runge-Kutta integration for efficient PDE-constrained LDDMM

Monica Hernandez

Computer Sciences Department
Aragon Institute on Engineering Research
University of Zaragoza
mhg@unizar.es

Abstract. The family of PDE-constrained LDDMM methods is emerging as a particularly interesting approach for physically meaningful diffeomorphic transformations. The original combination of Gauss–Newton–Krylov optimization and Runge-Kutta integration, shows excellent numerical accuracy and fast convergence rate. However, its most significant limitation is the huge computational complexity, hindering its extensive use in Computational Anatomy applied studies. This limitation has been treated independently by the problem formulation in the space of band-limited vector fields and Semi-Lagrangian integration. The purpose of this work is to combine both in three variants of band-limited PDE-constrained LDDMM for further increasing their computational efficiency. The accuracy of the resulting methods is evaluated extensively. For all the variants, the proposed combined approach shows a significant increment of the computational efficiency. In addition, the variant based on the deformation state equation is positioned consistently as the best performing method across all the evaluation frameworks in terms of accuracy and efficiency. This work was finished on January 2019 and is currently under review.

1 Introduction

Computational Anatomy is a powerful interdisciplinary field for the analysis of anatomical shape variability [1,2]. This discipline is based on Sir D’Arcy Thompson’s original ideas for explaining the similarity of the anatomical shape of homologous species using the transformations existing between the anatomical structures [3]. In Computational Anatomy, shape similarity is measured from the diffeomorphic transformations estimated between the anatomies. These transformations yield a generative model for the analysis of shape variability. Diffeomorphisms are computed from the anatomical images using diffeomorphic registration methods [4].

There exists a vast literature on diffeomorphic registration methods with differences in the transformation characterization, regularizers, image similarity metrics, optimization methods, and additional constraints [5]. Although the differentiability and invertibility of the transformations constitute crucial features for Computational Anatomy applications, the diffeomorphic constraint does not necessarily guarantee that a transformation computed with a given method is physically meaningful for the clinical domain of interest. PDE-constrained Large Deformation Diffeomorphic Metric Mapping (PDE-LDDMM) has become relevant in the last decade for the computation of transformations under plausible physical models of interest [6,7,8,9,10,11,12,13,14].

Our work focuses on the family of PDE-constrained LDDMM methods pioneered by Hart et al. [7] and leading to the relevant contributions in [10,11,15,16,17]. In this family of methods, the registration problem is approached from an optimal control perspective, where the different physical models are imposed directly using the physical PDEs that are attached to the LDDMM variational problem using hard constraints. The numerical optimization is approached using gradient-descent [7,10,15] or second-order optimization in the form of inexact reduced Newton-Krylov methods [10,11,16,17]. In particular, the combination of Gauss-Newton-Krylov for optimization, with sophisticated multi-level preconditioners, spectral methods for differentiation, and Runge-Kutta schemes for PDE integration, shows excellent numerical accuracy and an extraordinarily fast convergence rate. However, the most significant limitation of Gauss-Newton-Krylov PDE-constrained LDDMM is the huge computational complexity, which hinders the extensive use in Computational Anatomy applied studies. This computational complexity is due to:

1. The formulation of the problem in the spatial domain.
2. The large time-sampling needed for the stability of Runge-Kutta integration.

Both issues have been treated independently in the literature yielding to PDE-constrained LDDMM methods with increased efficiency and an assumable cost in accuracy loss.

1.1 Computational complexity due to problem formulation

The computational complexity due to the formulation of the problem in the spatial domain has been successfully reduced using the band-limited vector field

parameterization proposed in [18,13]. LDDMM methods, and in particular PDE-constrained LDDMM, involve the action of low-pass filters in the optimization update equations of the velocities. Therefore, the computation of the high-frequency components of high-resolution velocity fields can be omitted since these computations result equal or nearly equal to zero by the action of the low-pass filters. The band-limited vector field parameterization allows a reduction of the dimensionality of the problem that circumvents the high-frequency computations.

The works in [19,16] formulate three different variants of PDE-constrained LDDMM in the space of band-limited vector fields and perform the computations in the GPU. Some configurations of these variants have been really successful, greatly outperforming the state of the art methods in terms of computational complexity while keeping a competitive accuracy.

1.2 Computational complexity due to PDE integration

Runge-Kutta methods are explicit techniques. Hence they are only conditionally stable. This means that the time sampling should be selected enough to preserve the Courant-Friedrichs-Lewy (CFL) condition. For PDE-constrained LDDMM, the time sampling values that guarantee stability are usually large. As a result, the time and memory requirements of the problem are considerably increased. In particular, the memory requirements of PDE-constrained LDDMM is increased to limits that hinder the execution on limited memory devices such as the GPU. In addition, one can experience that the time-sampling needed for the non-stationary parameterization is much higher than for the stationary parameterization, increasing the complexity of an already not particularly memory efficient configuration. On the other side, when stability is satisfied, the accuracy of PDE-constrained LDDMM is high [10,11,19,16].

Semi-Lagrangian methods are semi-implicit techniques that are unconditionally stable. Therefore, the time sampling can be selected according to accuracy rather than stability considerations. Semi-Lagrangian methods were originally proposed in the 90's in the context of modelling weather predictions [20]. In the context of diffeomorphic registration, the original LDDMM method proposed in [21] already used Semi-Lagrangian integration for the solution of the transport equation. The combination of Semi-Lagrangian integration with Runge-Kutta has been recently proposed for solving some time-dependent PDEs. Runge-Kutta has shown to increase the accuracy of first-order schemes in Semi-Lagrangian integration [22].

The computational complexity in [10,11] due to the use of Runge-Kutta schemes for PDE integration has been successfully reduced using Semi-Lagrangian Runge-Kutta integration [23,17] for the stationary parameterization of diffeomorphisms. For PDE-constrained LDDMM, the selected time sampling is usually much smaller than the time sampling typically selected with explicit schemes, yielding to a considerable reduction of the computational complexity of the problem. On the other hand, the expected accuracy of PDE-constrained LDDMM is lower than with explicit schemes.

Beyond the computational complexity improvement through numerical schemes, Mang et al. proposed an efficient implementation of PDE-LDDMM that exploits massive CPU based parallel computing architectures [24]. The source code has been recently released with [17].

1.3 Our contribution

The purpose of this work is to further increase the computational efficiency of BL PDE-constrained LDDMM by combining the two independent methodological approaches of circumventing the huge computational complexity of PDE-constrained LDDMM and to extensively analyze the accuracy of the resulting methods. We have implemented the band-limited methods in [19,16] with the Semi-Lagrangian Runge-Kutta integration scheme originally proposed in [23] for the stationary and the non-stationary parameterization of diffeomorphisms. The resulting methods have been evaluated in five different datasets following the evaluation frameworks in [16,25,26]. To our knowledge, this is the first time that Semi-Lagrangian Runge-Kutta integration is implemented in the space of band-limited vector fields. It is also the first time that Semi-Lagrangian Runge-Kutta integration is used in PDE-LDDMM with the non-stationary parameterization. Moreover, our work first provides the position achieved by benchmark PDE-constrained LDDMM methods in the ranking of Klein et al. evaluation. The best performing method of our work coincides with the best performing variant in [16], PDE-constrained LDDMM based on the deformation state equation. The Semi-Lagrangian Runge-Kutta scheme proposed in this work has shown to outperform the Runge-Kutta scheme in [16] in terms of computational efficiency and accuracy. Indeed, the best performing PDE-LDDMM variant in this work has recently reached the highest sensitivity (97 % vs a baseline of 88 %) in the classification of stable vs progressive mild cognitive impaired converters in the Alzheimer’s Disease Neuroimaging Initiative (ADNI) database using convolutional neural networks [27].

1.4 Manuscript organization

In the following, Section 2 reviews the foundations of PDE-constrained LDDMM, with particular emphasis on the band-limited vector field parameterization. Section 3 presents the proposed Semi-Lagrangian Runge-Kutta integration method. Next, Section 4 details the experimental setup. Section 5 shows the results and Section 6 discusses the most important highlights. Finally, Section 7 gathers the most remarkable conclusions of our work.

2 PDE-constrained LDDMM methods

2.1 Parameterization in the spatial domain

Let $\Omega \subseteq \mathbb{R}^d$ be the image domain. Let $Diff(\Omega)$ be the LDDMM Riemannian manifold of diffeomorphisms and V the tangent space at the identity element.

$Diff(\Omega)$ is a Lie group, and V is the corresponding Lie algebra. The Riemannian metric of $Diff(\Omega)$ is defined from the scalar product in V

$$\langle v, w \rangle_V = \langle Lv, w \rangle_{L^2} = \int_{\Omega} \langle Lv(x), w(x) \rangle d\Omega, \quad (1)$$

where $L = (Id - \alpha\Delta)^s$, $\alpha > 0$, $s \in \mathbb{N}$ is the invertible self-adjoint differential operator associated with the differential structure of $Diff(\Omega)$ [21].

Let I_0 and I_1 be the source and the target images. PDE-constrained LDDMM is formulated from the minimization of the PDE-constrained variational problem

$$E(v) = \frac{1}{2} \int_0^1 \langle Lv_t, v_t \rangle_{L^2} dt + \frac{1}{\sigma^2} \|m(1) - I_1\|_{L^2}^2, \quad (2)$$

subject to the state equation with state variable $m(t)$

$$\partial_t m(t) + \nabla m(t) \cdot v_t = 0 \text{ in } \Omega \times (0, 1], \quad (3)$$

with initial condition $m(0) = I_0$ [7,10].

The variational problem is posed in the space of time-varying smooth flows of velocity fields, $v \in L^2([0, 1], V)$. Given the smooth flow $v : [0, 1] \rightarrow V$, $v_t : \Omega \rightarrow \mathbb{R}^d$, the solution at time $t = 1$ to the evolution equation

$$\partial_t \phi_t^v = v_t \circ \phi_t^v \quad (4)$$

with initial condition $\phi_0^v = id$ is a diffeomorphism, $\phi_1^v \in Diff(\Omega)$. The transformation $(\phi_1^v)^{-1}$, computed from the minimum of $E(v)$ constrained to the state equation, is the diffeomorphism that solves the PDE-constrained LDDMM registration problem between I_0 and I_1 .

The state equation constraint in PDE-constrained LDDMM can be imposed in two more different manners, yielding three different variants of PDE-constrained LDDMM [16]. The second variant is formulated from the minimization of Equation 2, where

$$m(t) = I_0 \circ \phi(t) \quad (5)$$

and ϕ is computed from the deformation state equation

$$\partial_t \phi(t) + D\phi(t) \cdot v_t = 0 \text{ in } \Omega \times (0, 1]. \quad (6)$$

The third variant is formulated from the minimization of Equation 2 subject to the deformation state equation (Equation 6).

The best optimization method for PDE-constrained LDDMM is Gauss-Newton-Krylov [10,16]. The expressions of the gradient and the Hessian-vector product are derived from the augmented Lagrangian of the energy functional and the state equation. The update equation has the form

$$v^{n+1} = v^n + \epsilon \delta v^n, \quad (7)$$

where ϵ is the update length and δv^n is computed from preconditioned conjugate gradient (PCG) on the system

$$H_v E_{aug}(v^n) \delta v^n = -\nabla_v E_{aug}(v^n), \quad (8)$$

with preconditioner L^{-1} .

2.2 Parameterization in the space of band-limited vector fields

Let $\tilde{\Omega}$ be the discrete Fourier domain truncated with frequency bounds K_1, \dots, K_d . We denote with \tilde{V} the space of discretized band-limited vector fields on Ω with these frequency bounds. The elements in \tilde{V} are represented in the Fourier domain as $\tilde{v} : \tilde{\Omega} \rightarrow \mathbb{C}^d$, $\tilde{v}(k_1, \dots, k_d)$. The application $\iota : \tilde{V} \rightarrow V$ denotes the natural inclusion mapping of \tilde{V} in V . The application $\pi : V \rightarrow \tilde{V}$ denotes the projection of V onto \tilde{V} [18,13].

The space \tilde{V} of band-limited vector fields has a finite-dimensional Lie algebra structure using the truncated convolution \star in the definition of the Lie bracket [13]. We denote with $Diff(\tilde{\Omega})$ to the finite-dimensional Riemannian manifold of diffeomorphisms on $\tilde{\Omega}$ with corresponding Lie algebra \tilde{V} . The Riemannian metric in $Diff(\tilde{\Omega})$ is defined from the scalar product

$$\langle \tilde{v}, \tilde{w} \rangle_{\tilde{V}} = \langle \tilde{L}\tilde{v}, \tilde{w} \rangle_{L^2}, \quad (9)$$

where \tilde{L} is the projection of operator L in the truncated Fourier domain. Similarly, we will denote with $\tilde{*}$ to the projection in the truncated Fourier domain of the differential operators $*$ involved in the differential equations.

The band-limited PDE-constrained variational problem is given by the minimization of

$$E(\tilde{v}) = \frac{1}{2} \int_0^1 \langle \tilde{L}\tilde{v}_t, \tilde{v}_t \rangle_{L^2} dt + \frac{1}{\sigma^2} \|m(1) - I_1\|_{L^2}^2. \quad (10)$$

The first variant is formulated from the minimization of Equation 10 subject to

$$\partial_t m(t) + \nabla m(t) \cdot \iota(\tilde{v}_t) = 0 \text{ in } \Omega \times (0, 1], \quad (11)$$

with initial condition $m(0) = I_0$. For the second variant, the diffeomorphism is computed from $\phi(t) = id - \iota(\tilde{u})(t)$ where $\tilde{u}(t)$ is computed from the deformation state equation formulated in displacement field form

$$\partial_t \tilde{u}(t) + \tilde{D}\tilde{u}(t) \star \tilde{v}_t = \tilde{u}(t) \text{ in } \tilde{\Omega} \times (0, 1]. \quad (12)$$

The third variant is formulated analogously to the spatial case from the minimization of Equation 10 subject to the deformation state equation (Equation 12) [19,16].

The optimization is approached using Gauss–Newton–Krylov methods in \tilde{V} with preconditioner \tilde{L}^{-1} . The update equation has the form

$$\tilde{v}^{n+1} = \tilde{v}^n + \epsilon \delta \tilde{v}^n, \quad (13)$$

where $\delta \tilde{v}^n$ is computed from

$$(H_{\tilde{v}} \widetilde{E_{aug}}(\tilde{v}^n)) \delta \tilde{v}^n = -(\nabla_{\tilde{v}} \widetilde{E_{aug}}(\tilde{v}^n)). \quad (14)$$

2.3 BL PDE-constrained LDDMM equations

Original BL PDE-constrained LDDMM Originally proposed BL PDE-constrained LDDMM uses the state equation in the augmented Lagrangian for the derivation of the state and adjoint equations and their incremental counterparts [19]. The gradient and the Gauss-Newton approximation of the Hessian-vector product are given by the equations

$$(\nabla_{\tilde{v}} \widetilde{E_{aug}}(\tilde{v}))_t = \tilde{L}\tilde{v}_t + \tilde{\lambda}(t) \star \tilde{\nabla} \tilde{m}(t) \quad (15)$$

$$(H_{\tilde{v}} \widetilde{E_{aug}}(\tilde{v}))_t \delta \tilde{v}(t) = \tilde{L} \delta \tilde{v}(t) + \delta \tilde{\lambda}(t) \star \tilde{\nabla} \tilde{m}(t), \quad (16)$$

where the projected state variable \tilde{m} and the projected adjoint variable $\tilde{\lambda}$ are computed from $\pi(m)$ and $\pi(\lambda)$, and m and λ are computed from

$$\partial_t m(t) + \nabla m(t) \cdot \iota(\tilde{v}_t) = 0 \quad (17)$$

$$-\partial_t \lambda(t) - \nabla \cdot (\lambda(t) \cdot \iota(\tilde{v}_t)) = 0. \quad (18)$$

The incremental counterparts $\delta \tilde{m}$ and $\delta \tilde{\lambda}$ are the solutions of

$$\partial_t \delta \tilde{m}(t) + \tilde{\nabla} \delta \tilde{m}(t) \star \tilde{v}_t + \tilde{\nabla} \tilde{m}(t) \star \delta \tilde{v}(t) = 0 \quad (19)$$

$$-\partial_t \delta \tilde{\lambda}(t) - \tilde{\nabla} \cdot (\delta \tilde{\lambda}(t) \star \tilde{v}_t) = 0 \quad (20)$$

in the BL domain. The initial conditions are, respectively, $m(0) = I_0$, $\lambda(1) = -\frac{2}{\sigma^2}(m(1) - I_1)$, $\delta \tilde{m}(0) = 0$, $\delta \tilde{\lambda}(1) = -\frac{2}{\sigma^2} \delta \tilde{m}(1)$.

BL PDE-constrained LDDMM based on the state equation This method departs from the original BL PDE-constrained LDDMM by using $m(t) = I_0 \circ \phi(t)$ and $\lambda(t) = J(t)\lambda(1) \circ \psi(t)$, where ψ is the inverse of ϕ , and J is the Jacobian determinant of ψ [7,16]. The transformations ϕ and ψ and the scalar field J are computed from the inclusion of the truncated displacement fields ($\tilde{u}(t)$ and $\tilde{v}(t)$) and the corresponding Jacobian

$$\phi(t) = id - \iota(\tilde{u}(t)), \quad (21)$$

$$\psi(t) = id - \iota(\tilde{v}(t)), \quad (22)$$

$$J(t) = 1 - \iota(\tilde{U}(t)), \quad (23)$$

where

$$\partial_t \tilde{u}(t) + \tilde{D}\tilde{u}(t) \star \tilde{v}_t = \tilde{v}_t \quad (24)$$

$$-\partial_t \tilde{v}(t) - \tilde{D}\tilde{v}(t) \star \tilde{v}_t = -\tilde{v}_t \quad (25)$$

$$-\partial_t \tilde{U}(t) - \tilde{v}_t \star \tilde{\nabla} \tilde{U}(t) = -\tilde{\nabla} \cdot \tilde{v} + \tilde{U}(t) \star \tilde{\nabla} \cdot \tilde{v}(t) \quad (26)$$

with initial conditions $\tilde{u}(0) = 0$, $\tilde{v}(1) = 0$, and $\tilde{U}(1) = 0$.

The incremental state and adjoint variables are computed from

$$\delta m(t) = \nabla I_0 \circ \phi(t) \cdot \iota(\delta \tilde{u}(t)) \quad (27)$$

$$\delta \lambda(t) = J(t) \nabla \lambda(1) \circ \psi(t) \cdot \iota(\delta \tilde{v}(t)) \quad (28)$$

where $\delta\tilde{u}$ and $\delta\tilde{v}$ are computed from

$$\partial_t\delta\tilde{u}(t) + \tilde{D}\delta\tilde{u}(t) \star \tilde{v}_t + \tilde{D}\tilde{u}(t) \star \delta\tilde{v}_t = \delta\tilde{v}_t \quad (29)$$

$$-\partial_t\delta\tilde{v}(t) - \tilde{D}\delta\tilde{v}(t) \star \tilde{v}_t - \tilde{D}\tilde{v}(t) \star \delta\tilde{v}_t = -\delta\tilde{v}_t \quad (30)$$

with initial conditions $\delta\tilde{u}(0) = 0$ and $\delta\tilde{v}(1) = 0$.

BL PDE-constrained LDDMM based on the deformation state equation The third method is formulated from the minimization of Equation 10 subject to the truncated displacement state equation [16]

$$\partial_t\tilde{u}(t) + \tilde{D}\tilde{u}(t) \star \tilde{v}_t = \tilde{v}_t. \quad (31)$$

The gradient and the Hessian-vector product are given by the equations

$$(\nabla_{\tilde{v}}\widetilde{E_{aug}}(\tilde{v}))_t = \tilde{L}\tilde{v}_t + \tilde{\rho}(t) - \tilde{D}\tilde{u}(t) \star \tilde{\rho}(t) \quad (32)$$

$$(H_{\tilde{v}}\widetilde{E_{aug}}(\tilde{v}))_t\delta\tilde{v}(t) = \tilde{L}\delta\tilde{v}(t) + \delta\tilde{\rho}(t) - \tilde{D}\delta\tilde{u}(t) \star \tilde{\rho}(t), \quad (33)$$

where the displacement state variable \tilde{u} , the adjoint variable $\tilde{\rho}$, and their incremental counterparts $\delta\tilde{u}$ and $\delta\tilde{\rho}$ are computed from

$$\partial_t\tilde{u}(t) + \tilde{D}\tilde{u}(t) \star \tilde{v}_t = \tilde{v}_t \quad (34)$$

$$-\partial_t\tilde{\rho}(t) - \widetilde{\nabla}\cdot(\tilde{\rho}(t) \star \tilde{v}_t) = 0 \quad (35)$$

$$\partial_t\delta\tilde{u}(t) + \tilde{D}\delta\tilde{u}(t) \star \tilde{v}_t + \tilde{D}\tilde{u}(t) \star \delta\tilde{v}(t) = \delta\tilde{v}(t) \quad (36)$$

$$-\partial_t\delta\tilde{\rho}(t) - \widetilde{\nabla}\cdot(\delta\tilde{\rho}(t) \star \tilde{v}_t) = 0 \quad (37)$$

with initial conditions $\tilde{u}(0) = 0$, $\tilde{\rho}(1) = \pi(-\frac{2}{\sigma^2}(m(1) - I_1)\nabla m(1))$, $\delta\tilde{u}(0) = 0$, and $\delta\tilde{\rho}(1) = \pi(-\frac{2}{\sigma^2}\delta m(1)\nabla m(1))$.

3 Semi-Lagrangian Runge-Kutta integration

3.1 Semi-Lagrangian integration in a spatial domain

Semi-Lagrangian (SL) integration methods [20] allow solving transport equations of the general form

$$D_t u = f(u, v), \quad (38)$$

where $u : \Omega^d \times [0, 1] \rightarrow \mathbb{R}$ is a scalar or a vector function varying in time, and

$$D_t u = \partial_t u + Du \cdot v.$$

SL methods combine the most interesting properties of Eulerian and Lagrangian schemes. On the one hand, SL methods involve following the characteristic lines of the differential equation, similarly to Lagrangian approaches. On the other hand, the equation is solved on the regular grid, similarly to Eulerian approaches.

As a result, SL methods are unconditionally stable as Lagrangian schemes. This means that the time sampling can be selected according to accuracy considerations rather than stability considerations. SL methods allow selecting a time sampling usually much smaller than Eulerian methods yielding a sensible reduction of the computational complexity.

SL schemes involve two steps. First, the departure points are computed solving the characteristic equation

$$D_t X(t) = v(t, X(t)), \quad (39)$$

with initial condition $X(0) = x$. The direction of the time integration can be forward or backward, depending on the direction of the time integration of the transport equation. From the several methods proposed in the literature for solving the characteristic equation, we use the approach given by Mang et al. in [23]

$$X_* = x - \delta t \cdot v \quad (40)$$

$$v_* = v \circ X_* \quad (41)$$

$$X_* = x - 0.5 \delta t \cdot (v_* + v). \quad (42)$$

Second, the transport equation (Equation 38) is solved in the Eulerian grid

$$D_t u(X(t), t) = f(u(X(t), t), v(t, X(t))) \quad (43)$$

along the characteristic line X . The use of Runge-Kutta (RK) integration has been recently proposed in this step, yielding a higher-order accurate SL-RK method [22]. The velocity field needs to be estimated at points that do not belong to the Eulerian grid. Therefore, an interpolator is needed. Cubic interpolation is the method of choice for SL schemes [28].

3.2 Semi-Lagrangian integration in a band-limited domain

In $\tilde{\Omega}$, the transport equations are of the general form

$$\tilde{D}_t \tilde{u} = \tilde{f}(\tilde{u}, \tilde{v}), \quad (44)$$

where

$$\tilde{D}_t \tilde{u} = \partial_t \tilde{u} + \tilde{D} \tilde{u} \star \tilde{v}. \quad (45)$$

The characteristics are computed from

$$D_t X(t) = \iota(\tilde{v})(t, X(t)), \quad (46)$$

and the transport equation is solved from

$$\tilde{D}_t \tilde{u}(\tilde{X}(t), t) = \tilde{f}(\tilde{u}(\tilde{X}(t), t), \tilde{v}(t, \tilde{X}(t))). \quad (47)$$

Equation in original form	Equation in SL form
$\partial_t m(t) + \nabla m(t) \cdot \iota(\tilde{v}_t) = 0$ (eq. 17)	$D_t m(t) = 0$
$-\partial_t \lambda(t) - \nabla \cdot (\lambda(t) \cdot \iota(\tilde{v}_t)) = 0$ (eq. 18)	$-D_t \lambda(t) = \lambda(t) \nabla \cdot \iota(\tilde{v}_t)$
$\partial_t \tilde{u}(t) + \tilde{D} \tilde{u}(t) \star \tilde{v}_t = \tilde{v}_t$ (eq. 24)	$\tilde{D}_t \tilde{u}(t) = \tilde{v}_t$
$-\partial_t \tilde{\rho}(t) - \tilde{\nabla} \cdot (\tilde{\rho}(t) \star \tilde{v}_t) = 0$ (eq. 35)	$-\tilde{D}_t \tilde{\rho}(t) = \tilde{\rho}(t) \star \tilde{\nabla} \cdot \tilde{v}_t$
$\partial_t \delta \tilde{m}(t) + \tilde{\nabla} \delta \tilde{m}(t) \star \tilde{v}_t + \tilde{\nabla} \tilde{m}(t) \star \delta \tilde{v}(t) = 0$ (eq. 19)	$\tilde{D}_t \delta \tilde{m}(t) = -\tilde{\nabla} \tilde{m}(t) \star \delta \tilde{v}_t$
$-\partial_t \delta \tilde{\lambda}(t) - \tilde{\nabla} \cdot (\delta \tilde{\lambda}(t) \star \tilde{v}_t) = 0$ (eq. 20)	$-D_t \delta \tilde{\lambda}(t) = \tilde{\lambda}(t) \star \tilde{\nabla} \cdot \tilde{v}_t$
$\partial_t \delta \tilde{u}(t) + \tilde{D} \delta \tilde{u}(t) \star \tilde{v}_t + \tilde{D} \tilde{u}(t) \star \delta \tilde{v}(t) = \delta \tilde{v}(t)$ (eq. 29)	$\tilde{D}_t \delta \tilde{u}(t) = \delta \tilde{v}_t - \tilde{D} \tilde{u}(t) \star \delta \tilde{v}(t)$
$-\partial_t \delta \tilde{\rho}(t) - \tilde{\nabla} \cdot (\delta \tilde{\rho}(t) \star \tilde{v}_t) = 0$ (eq. 37)	$-\tilde{D}_t \delta \tilde{\rho}(t) = \delta \tilde{\rho}(t) \star \tilde{\nabla} \cdot \tilde{v}_t$

Table 1. Original PDEs involved in BL PDE-constrained LDDMM and corresponding PDEs written in SL form.

3.3 Semi-Lagrangian Runge-Kutta integration in PDE-LDDMM

In this work, SL-RK integration has been implemented in Ω and $\tilde{\Omega}$ for the spatial and band-limited versions of the three PDE-LDDMM variants. To be able to apply SL integration, the differential equations need to be written in the shape of equations 43 or 47. We focus on the derivation for the BL domain $\tilde{\Omega}$. The derivation for the spatial domain can be performed analogously.

The state equations, the deformation state equations, and their incremental counterparts (Equations 17, 24, 19, 29) are already in the shape of equation 47 by just moving to the right-hand-side of the equation a remaining term. For the adjoint and the incremental adjoint equations (Equations 18, 35, 20, 37) we use the identity

$$\tilde{\nabla} \cdot (\tilde{u} \star \tilde{v}) = \tilde{u} \tilde{\nabla} \cdot \tilde{v} + \tilde{v} \star \tilde{\nabla} \tilde{u} \text{ in } \tilde{\Omega} \quad (48)$$

and move the divergence term to the right-hand-side of the transformed equation. Table 1 gathers the expressions of the resulting differential equations, needed for the implementation of BL PDE-constrained LDDMM methods in SL form. For SL-RK, the right-hand side expressions can be directly plugged into an RK differential solver.

4 Experimental setup

In this work, we evaluate the performance of SL-RK integration in all the variants of PDE-constrained LDDMM (see Table 2). The evaluation has been performed consistently with our previous work [19,16], in order to show the improvement of the proposed integration method over RK integration. In addition, we have performed an extensive evaluation of the most memory efficient stationary methods in the frameworks of Klein et al. [25] and Rohlfing et al. [26] in order to establish the position achieved by PDE-constrained LDDMM methods in these evaluation rankings.

Abbreviation	Method	Integration	Publication
PDE-LDDMM RK	PDE-constrained LDDMM	RK	Mang et al. [10]
PDE-LDDMM st. eq. RK	PDE-constrained LDDMM based on the state equation	RK	Hernandez [16]
PDE-LDDMM def. eq. RK	PDE-constrained LDDMM based on the deformation state equation	RK	Hernandez [16]
PDE-LDDMM SL	PDE-constrained LDDMM	SL-RK	Mang et al. [23]
PDE-LDDMM st. eq. SL	PDE-constrained LDDMM based on the state equation	SL-RK	this work
PDE-LDDMM def. eq. SL	PDE-constrained LDDMM based on the deformation state equation	SL-RK	this work
BL PDE-LDDMM RK	band-limited PDE-constrained LDDMM	RK	Hernandez [19]
BL PDE-LDDMM st. eq. RK	band-limited PDE-constrained LDDMM based on the state equation	RK	Hernandez [16]
BL PDE-LDDMM def. eq. RK	band-limited PDE-constrained LDDMM based on the deformation state equation	RK	Hernandez [16]
BL PDE-LDDMM SL	band-limited PDE-constrained LDDMM	SL-RK	this work
BL PDE-LDDMM st. eq. SL	band-limited PDE-constrained LDDMM based on the state equation	SL-RK	this work
BL PDE-LDDMM def. eq. SL	band-limited PDE-constrained LDDMM based on the deformation state equation	SL-RK	this work

Table 2. List of the PDE-constrained LDDMM methods compared in this work. The table gathers the abbreviations used in this experimental section, the name of the method given in Section 2, the integration scheme, and the publication where the method first appeared.

4.1 Datasets

We have used five different databases in our evaluation:

NIREP16 contains 16 skull-stripped brain images with the segmentation of 32 gray matter structures. The dimension of the images is $256 \times 300 \times 256$ with a voxel size of $0.7 \times 0.7 \times 0.7$ mm. The acquisition and post-processing details can be found at the web page <http://www.nirep.org>. The most remarkable features of this dataset are the excellent image quality and the ventricle sizes that are usually small. The geometry of the segmentations provides a specially challenging framework for deformable registration evaluation.

LPBA40 contains 40 skull-stripped brain images without the cerebellum and the brain stem. LPBA40 is provided with the segmentation of 50 gray matter structures together with the caudate, putamen, and hippocampus. LPBA40 protocols can be found at

<http://www.loni.ucla.edu/Protocols/LPBA40>. The image quality in LPBA40 is, overall, acceptable. The variability of the ventricle sizes is high.

IBSR18 contains 18 brain images with the segmentation of 96 cerebral structures. The masks for skull-stripping are available with the dataset. In addition, the release **IBSR_V2.0** skull-stripped NIFTI [26] contains 18 skull-stripped brain images with the segmentation of 62 cerebral structures. This dataset provides the segmentation of brain structures of interest for the evaluation of image registration methods. The image quality is low. For example, most of the images show motion artifacts. The variability of the ventricle sizes is high.

CUMC12 contains 12 full brain images with the segmentation of 130 cerebral structures. The masks for skull-stripping are available with the dataset. Overall, the image quality is acceptable, although some of the images are noisy. The contrast of the images is low. The variability of the ventricle sizes is high.

MGH10 contains 10 full brain images with the segmentation of 106 cerebral structures. The masks for skull-stripping are available with the dataset. Overall, the image quality is acceptable, although some of the images are noisy. The contrast of the images is low. Ventricle sizes are usually all big.

4.2 Image registration pipeline

The evaluation consistent with our previous work was performed in a subsampled NIREP16 database. The registrations were carried out from the first subject to every other subject in the database, yielding to a total of 15 registrations per method. The subsampled NIREP16 database was obtained from the resampling of the images into volumes of size $180 \times 210 \times 180$ with a voxel size of $1.0 \times 1.0 \times 1.0$ mm after the alignment to a common coordinate system using affine transformations. The images were scaled between 0 and 1. The affine alignment and subsampling were performed using the Insight Toolkit (ITK). The PDE-constrained registration methods were executed directly on this dataset. For benchmarking, we run single- and multi-resolution versions of the SyN version of ANTS diffeomorphic registration [29] with L^2 image similarity (ANTS-SSD).

The evaluation in the framework of Klein et al. was performed in NIREP16, LPBA40, IBSR18, CUMC12, and MGH10 databases. The IBSR18, CUMC12 and MGH10 images normalized with respect to the MNI152 space were used as input data. The registrations were carried out from every subject to every other subject in each database yielding to a total of 2154 registrations per method. The evaluation in the framework of Rohlfing et al. was performed in IBSR18 database, with a total of 306 registrations per method. The NIREP16, LPBA40, IBSR18, CUMC12, and MGH10 images were preprocessed similarly to [25]. In the first place, N4 bias field correction and histogram matching were applied to all the images. To perform these preprocessing steps we used the algorithms available in ITK. The images were scaled between 0 and 1. Next, we performed an affine registration between all the image pairs. Instead of using the affine registered images as input of our non-rigid registration methods, we used the affine transformation as input, and it was included in the parameterization of the diffeomorphic transformations.

Subsampled NIREP experiments were run on a cluster equipped with one NVidia Titan RTX with 24 GBS of video memory and an Intel Core i7 with

64 GBS of DDR3 RAM. NIREP16, LPBA40, IBSR18, CUMC12, and MGH10 experiments were run on a cluster equipped with four NVidia GeForce GTX 1080 ti with 11 GBS of video memory and an Intel Core i7 with 64 GBS of DDR3 RAM. The codes were developed in the GPU with Matlab 2017a and Cuda 8.0. Since Matlab lacks a 3D GPU cubic interpolator, we implemented in a Cuda MEX file the GPU cubic interpolator with prefiltering proposed in [30].

4.3 Parameter configuration

Regularization parameters were selected from a search of the optimal parameters in the registration experiments performed in our previous work [16]. We selected the parameters $\sigma^2 = 1.0$, $\alpha = 0.0025$, and $s = 2$.

The optimization was run a maximum of 10 iterations with the stopping conditions used in [10]. The maximum number of PCG iterations was selected equal to 5. These parameters were selected as optimal in our previous work since the methods achieved state of the art accuracy at a reasonable amount of time [19].

The experiments were performed with band sizes of $32 \times 32 \times 32$ for BL PDE-constrained LDDMM based on the state and on the deformation state equations, and band sizes of $40 \times 40 \times 40$ for original BL PDE-constrained LDDMM. This selection was found as optimal for each method in our previous work [19,16].

For SL-RK integration, n_t was selected equal to 5 for all the methods. For RK integration, n_t was selected equal to 25 for the BL PDE-constrained LDDMM based on the state and on the deformation state equations, and 50 for the spatial methods due to stability issues. In the evaluation with LPBA40, IBSR18, CUMC12, and MGH10 datasets, $n_t = 25$ showed stability issues in a considerable number of experiments and it was raised to 50.

ANTS-SSD was run with the following parameters for the single-resolution experiments

```
$synconvergence="[50,1e-6,10]",
$synshrinkfactors="1",
and $synsmoothingsigmas="3vox".
```

For the multi-resolution experiments the parameters were set to

```
$synconvergence="[50x50x50,1e-6,10]",
$synshrinkfactors="4x2x1",
and $synsmoothingsigmas="3x2x1vox".
```

The selection of the number of iterations was in agreement with the number of outer \times inner iterations used in Gauss–Newton–Krylov optimization.

5 Results

5.1 Subsampled NIREP16 evaluation results

Convergence analysis Table 3 shows, averaged by the number of experiments, the mean and standard deviation of the relative image similarity error after

Method	n_t	MSE_{rel}	$\ g\ _{\infty,rel}$	$\min(J(\phi_1^v)^{-1})$	$\max(J(\phi_1^v)^{-1})$
St. PDE-LDDMM RK	50	18.29 ± 2.83	0.07 ± 0.05	0.16 ± 0.05	3.70 ± 0.51
St. PDE-LDDMM st. eq. RK	30	18.42 ± 2.71	0.18 ± 0.19	0.07 ± 0.06	2.95 ± 0.41
St. PDE-LDDMM def. st. eq. RK	30	16.83 ± 1.53	0.16 ± 0.08	0.12 ± 0.05	4.12 ± 1.41
St. PDE-LDDMM SL	5	19.55 ± 1.76	0.14 ± 0.13	0.03 ± 0.04	3.25 ± 0.29
St. PDE-LDDMM st. eq. SL	5	18.34 ± 1.68	0.23 ± 0.21	0.03 ± 0.04	3.46 ± 0.69
St. PDE-LDDMM def. st. eq. SL	5	17.10 ± 1.50	0.12 ± 0.05	0.14 ± 0.05	5.02 ± 1.01
NSt. PDE-LDDMM RK	50	22.68 ± 5.49	0.26 ± 0.12	0.16 ± 0.05	3.38 ± 0.90
NSt. PDE-LDDMM, st. eq. RK	25*	29.92 ± 2.41	0.32 ± 0.10	0.11 ± 0.07	2.93 ± 0.78
NSt. PDE-LDDMM, def. st. eq. RK	30	16.10 ± 1.70	0.20 ± 0.08	0.09 ± 0.03	4.55 ± 0.69
NSt. PDE-LDDMM SL	5	22.44 ± 6.26	0.51 ± 0.18	0.02 ± 0.02	3.96 ± 0.65
NSt. PDE-LDDMM st. eq. SL	5	21.82 ± 2.51	0.49 ± 0.19	0.01 ± 0.02	4.20 ± 0.94
NSt. PDE-LDDMM def. st. eq. SL	5	16.86 ± 1.91	0.13 ± 0.04	0.09 ± 0.02	7.35 ± 2.63
BL St. PDE-LDDMM 40x RK	25	20.99 ± 2.59	0.04 ± 0.03	0.21 ± 0.04	3.32 ± 0.41
BL St. PDE-LDDMM st. eq. 32x RK	25	18.53 ± 1.71	0.02 ± 0.01	0.11 ± 0.07	3.10 ± 0.35
BL St. PDE-LDDMM def. st. eq. 32x RK	25	17.32 ± 1.68	0.03 ± 0.01	0.13 ± 0.05	3.76 ± 0.49
BL St. PDE-LDDMM 40x SL	5	20.41 ± 1.89	0.02 ± 0.00	0.32 ± 0.02	9.65 ± 4.77
BL St. PDE-LDDMM st. eq. 32x SL	5	19.89 ± 1.76	0.01 ± 0.00	0.29 ± 0.03	7.94 ± 2.81
BL St. PDE-LDDMM def. st. eq. 32x SL	5	17.77 ± 1.66	0.04 ± 0.01	0.21 ± 0.03	8.23 ± 3.24
BL NSt. PDE-LDDMM 40x RK	25	29.30 ± 3.50	0.21 ± 0.08	0.24 ± 0.05	2.25 ± 0.51
BL NSt. PDE-LDDMM, st. eq. 32x RK	25	29.21 ± 3.96	0.24 ± 0.11	0.15 ± 0.06	2.71 ± 0.48
BL NSt. PDE-LDDMM, def. st. eq. 32x RK	25	15.68 ± 1.52	0.04 ± 0.01	0.09 ± 0.04	4.77 ± 0.78
BL NSt. PDE-LDDMM 40x SL	5	19.14 ± 2.06	0.11 ± 0.05	0.01 ± 0.07	5.25 ± 0.80
BL NSt. PDE-LDDMM st. eq. 32x SL	5	20.49 ± 1.75	0.17 ± 0.15	0.07 ± 0.03	4.51 ± 0.61
BL NSt. PDE-LDDMM def. st. eq. 32x SL	5	16.80 ± 1.57	0.07 ± 0.03	0.09 ± 0.03	7.37 ± 1.43

Table 3. Subsampled NIREP16. Convergence results. Mean and standard deviation of the relative image similarity error expressed in % (MSE_{rel}), the relative gradient magnitude ($\|g\|_{\infty,rel}$), and the Jacobian determinant extrema associated with the transformation $(\phi_1^v)^{-1}$. St. stands for the stationary and NSt. for the non-stationary parameterization of diffeomorphisms. (*) The n_t selected for NSt. PDE-LDDMM, st. eq. with RK integration was due to a memory load greater than the GPU maximum capacity (24 GBS).

registration,

$$MSE_{rel} = \frac{\|m(1) - I_1\|_{L^2}^2}{\|I_0 - I_1\|_{L^2}^2},$$

the relative gradient magnitude,

$$\|g\|_{\infty,rel} = \frac{\|\nabla_v E(v^n)\|_{\infty}}{\|\nabla_v E(v^0)\|_{\infty}},$$

and the extrema of the Jacobian determinant obtained with PDE-constrained LDDMM in the subsampled NIREP16 dataset.

We have grouped the analysis of the MSE_{rel} values by integration scheme, variant, image domain, and diffeomorphism parameterization:

- RK vs SL-RK. The MSE_{rel} value achieved by SL-RK methods is close or improves RK methods. It drives our attention the bad performance of PDE-LDDMM st. eq. for the non-stationary parameterization and RK integration which is indeed improved by SL-RK integration.
- Variants. The best performing variant is PDE-LDDMM def. st. eq. This result is persistent for the different integration schemes, the spatial or BL parameterization, and the diffeomorphic parameterization.
- SP vs BL. The MSE_{rel} values obtained with the spatial methods are slightly degraded by the BL methods as expected. The degradation is only shown in some cases.
- St. vs NST. The non-stationary methods do not outperform the stationary methods in a consistent manner. The (out)performance depends on the variant.

For the bad-performing methods, the high values of the relative gradient indicate the stagnation of the convergence. For the BL methods, the relative gradient was reduced to average values ranging from 0.02 to 0.04, which means that the optimization was stopped in acceptable energy values in all cases. All the Jacobians remained above zero.

Evaluation The evaluation is based on the accuracy of the registration results for template-based segmentation. The Dice Similarity Coefficient (DSC) is selected as the evaluation metric. Given two segmentations S and T , the DSC is defined as

$$DSC(S, T) = \frac{2\text{Vol}(S \cap T)}{\text{Vol}(S) + \text{Vol}(T)}. \quad (49)$$

This metric provides the value of 1 if S and T exactly overlap and gradually decreases towards 0 depending on the overlap of the two volumes.

Figure 1 shows, in the shape of box and whisker plots, the statistical distribution of the DSC values obtained after the registration across the 32 segmented structures. For the single-resolution experiments, the performance of the benchmark method ANTS-SSD was under 50%. For the multi-resolution experiments, the average DSC value achieved by ANTS-SSD equals to 55.59%. We have selected this value as a baseline of good registration accuracy for methods with L^2 -based image similarity.

A great number of PDE-LDDMM methods showed similar values or even improved ANTS-SSD performance. The best performing variant was our PDE-LDDMM based on the deformation state equation (boxes in pink tones). This variant showed similar results for RK and SL-RK integration regardless the image domain and diffeomorphism parameterization.

For the variant associated with the PDE-constrained benchmark methods [10,23] (boxes in blue tones), RK integration slightly outperformed SL-RK integration for the stationary parameterization. For the non-stationary parameterization

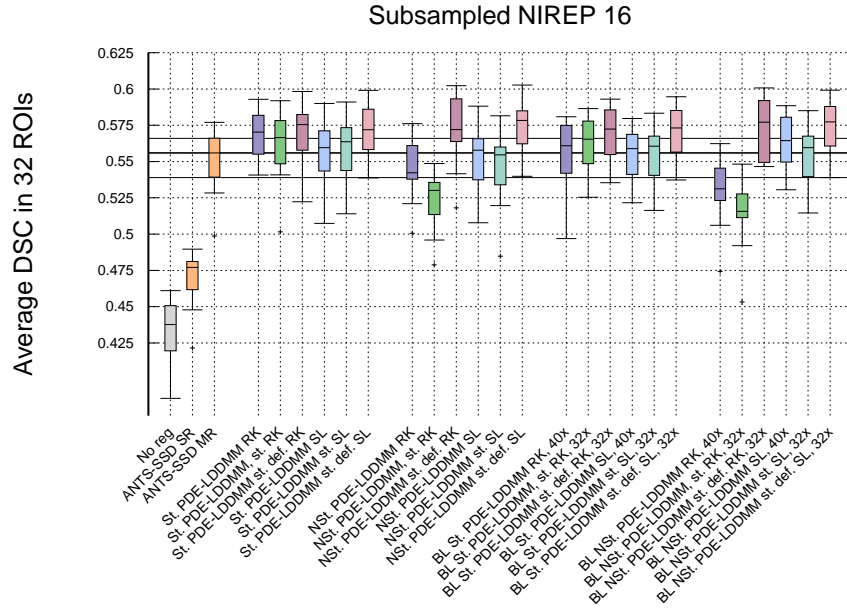


Fig. 1. Subsampled NIREP16. Volume overlap obtained by the registration methods measured in terms of the DSC between the warped and the corresponding manual target segmentations. Box and whisker plots show the distribution of the DSC values averaged over the 32 NIREP manual segmentations. The whiskers indicate the minimum and maximum of the DSC values. The horizontal lines in the plot indicate the first, second, and third quartiles of multi-resolution ANTS-SSD.

the median DSC value for RK integration was under the value for SL-RK integration. Similarly, RK slightly outperformed SL-RK integration for BL PDE-LDDMM and BL PDE-LDDMM based on the state equation for the stationary parameterization. On the contrary, SL-RK integration greatly outperformed RK integration for the non-stationary parameterization.

The variant based on the state equation (boxes in green tones) performed similarly to benchmark PDE-LDDMM variant for the stationary parameterization for the same integration scheme. However, it is remarkable the low performance achieved by this variant for the non-stationary parameterization and RK integration in both image domains.

Method	Integration	VRAM (MBS)	total time (s)
St. PDE-LDDMM	RK	10311	2281.40 \pm 378.56
St. PDE-LDDMM st. eq.	RK	17229	877.85 \pm 176.03
St. PDE-LDDMM def. st. eq.	RK	15321	1298.50 \pm 151.19
St. PDE-LDDMM	SL-RK	3901	118.29 \pm 4.77
St. PDE-LDDMM st. eq.	SL-RK	6267	139.91 \pm 22.06
St. PDE-LDDMM def. st. eq.	SL-RK	5935	221.01 \pm 2.40
NSt. PDE-LDDMM	RK	14913	3443.17 \pm 932.45
NSt. PDE-LDDMM, st. eq.	RK	20635	816.79 \pm 480.61
NSt. PDE-LDDMM, def. st. eq.	RK	19065	2222.04 \pm 369.96
NSt. PDE-LDDMM	SL-RK	11155	191.96 \pm 45.53
NSt. PDE-LDDMM st. eq.	SL-RK	12429	214.09 \pm 48.54
NSt. PDE-LDDMM def. st. eq.	SL-RK	12065	355.47 \pm 4.38
BL St. PDE-LDDMM 40x	RK	5709	312.45 \pm 5.22
BL St. PDE-LDDMM st. eq. 32x	RK	4743	315.00 \pm 2.73
BL St. PDE-LDDMM def. st. eq. 32x	RK	1819	377.56 \pm 4.26
BL St. PDE-LDDMM 40x	SL-RK	2685	68.66 \pm 1.32
BL St. PDE-LDDMM st. eq. 32x	SL-RK	2877	80.76 \pm 0.35
BL St. PDE-LDDMM def. st. eq. 32x	SL-RK	2365	116.99 \pm 1.04
BL NSt. PDE-LDDMM 40x	RK	6657	825.15 \pm 19.93
BL NSt. PDE-LDDMM, st. eq. 32x	RK	4789	535.52 \pm 279.65
BL NSt. PDE-LDDMM, def. st. eq. 32x	RK	1863	905.48 \pm 25.13
BL NSt. PDE-LDDMM 40x	SL-RK	6131	158.79 \pm 15.29
BL NSt. PDE-LDDMM st. eq. 32x	SL-RK	6171	159.49 \pm 20.59
BL NSt. PDE-LDDMM def. st. eq. 32x	SL-RK	5577	249.60 \pm 10.85

Table 4. Computational complexity, GPU peak memory usage and mean and standard deviation of the total computation time. Experiments run in an NVidia Titan RTX with 24 GBS of video memory.

Computational complexity Table 4 shows the VRAM peak memory reached through the computations, and the average and standard deviation of the total computation time in the subsampled NIREP16 experiments. For the spatial methods, SL-RK integration achieved a substantial time and memory reduction over RK integration. The time and memory reduction achieved by SL-RK over RK integration was also considerable for the BL parameterized methods. For the stationary parameterization, the BL parameterization further decreased the complexity of spatial SL-RK integration methods, as expected. However, SL-RK integration did not reduce the memory VRAM usage for the non-stationary parameterization while the total computation time was effectively reduced.

Qualitative assessment For a qualitative assessment of the proposed registration methods, we show the registration results obtained by Mang et al. benchmark methods [10,12], and PDE-LDDMM based on the deformation state equation in a selected experiment representative of a difficult deformable registration problem. For the non-stationary parameterization the images for a qualitative assessment were similar to the stationary parameterization. Figure ?? shows the warped images, the difference between the warped and the target images after registration, and the velocity field.

5.2 NIREP16, LPBA40, IBSR18, CUMC12, and MGH10 evaluation results

From the evaluation measurements used in Klein et al. framework, we focus on the accuracy of the registration results for template-based segmentation. Since [25], this has been adopted as a widely extended criterion for non-rigid registration evaluation. From the metrics proposed in [25], we select the Dice Similarity Coefficient (DSC) as evaluation metric. Figures 2, 3 and 4 show the statistical distribution of the DSC values obtained after the registration across the manually segmented structures for the five databases. For the NIREP16 dataset, we show the results obtained with ANTS-SSD. For the remaining databases, we include the results reported in [25] for affine registration (FLIRT), and three diffeomorphic registration methods: Diffeomorphic Demons, SyN, and Dartel.

On the one hand, the results from NIREP16 show how PDE-LDDMM based on the deformation state equation outperformed the other variants of PDE-constrained LDDMM. The distribution of the method parameterized in the BL domain resulted almost identical to the distribution of the method parameterized in the spatial domain. As happened with subsampled NIREP16 evaluation, ANTS-SSD was among the worst performing methods. BL PDE-LDDMM and BL PDE-LDDMM based on the state equation with RK integration exceeded the maximum VRAM capacity of our GPUs for this dataset.

On the other hand, the results from LPBA40, IBSR18, CUMC12, and MGH10 show that, from the PDE-constrained LDDMM methods, the best performing method was BL PDE-LDDMM based on the deformation state equation and SL-RK integration. The performance of the method with RK integration

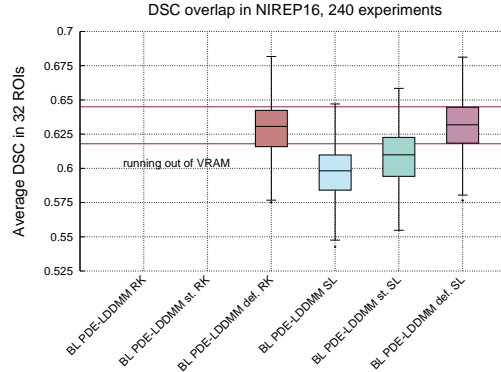


Fig. 2. NIREP16. Distribution of the DSC values averaged over the 32 NIREP manual segmentations in the 240 experiments. The whiskers indicate the minimum and maximum of the DSC values. The methods running out of 11 GBS VRAM are indicated in the plots. The horizontal red lines indicate the first and third quartiles of BL PDE-LDDMM based on the deformation state equation.

was slightly lower. The performance of original PDE-LDDMM, PDE-LDDMM based on the state equation and their BL versions was significantly lower in IBSR18, CUMC12, and MGH10 databases. For these methods, RK integration performed slightly better than SL-RK integration. These results are consistent with NIREP16 evaluation results.

In IBSR18, CUMC12, and MGH10 databases, our PDE-constrained LDDMM methods were not able to reach SyN or Dartel performance. This is probably because the image similarity metrics used in these methods (Cross-Correlation and multinomial model, respectively) favour the accuracy in template-based segmentation. In contrast, PDE-constrained LDDMM uses SSD, which is known to restrict the performance in template-based segmentation. However, in LPBA40 databases, our best performing PDE-constrained LDDMM methods overpass Dartel and almost reached SyN performance, while showing a significantly reduced number of outliers.

Our methods significantly outperformed FLIRT and Diffeomorphic Demons, where the third quartile in the distribution of our best performing method was close to the median of Demons for the four databases. It should be noticed that Diffeomorphic Demons also uses SSD as image similarity metric.

5.3 IBSR18 V2.0 evaluation results

Figure 5 shows the statistical distribution of the DSC values obtained by our proposed registration methods in the regions of interest of Rohlfing et al. evaluation framework [26]. Consistently with the rest of the evaluation results, the best performing method was BL PDE-LDDMM based on the deformation state

equation, which significantly outperformed the others in the great majority of regions.

6 Discussion

The increase of the computational efficiency achieved by the combined over the split BL and SL-RK approaches was significant in terms of computation time and memory. The reduction of the memory requirements allowed us to perform the evaluation of the SL-RK PDE-constrained LDDMM methods extensively, even in the highest-resolution level of NIREP16.

In all the evaluation frameworks, BL PDE-constrained LDDMM based on the deformation state equation with SL-RK integration resulted our best performing method. This method achieved an identical DSC distribution compared with RK integration in the NIREP16 database. In NIREP16 database, the method greatly outperformed ANTS-SSD. In LPBA40, IBSR18, CUMC12, and MGH10 databases, the method outperformed Diffeomorphic Demons. In addition, the evaluation results in the regions of interest of Rohlfing et al. corroborated its excellent performance.

For Mang et al. benchmark PDE-constrained LDDMM methods [10,23], our evaluation results reported a significant loss of accuracy between RK and SL-RK integration. Interestingly, this loss of accuracy was not observed for our best performing method.

In IBSR18, CUMC12, and MGH10 databases, our PDE-constrained LDDMM methods were not able to reach SyN or Dartel performance. This is because SSD image similarity metric restricts the performance of the methods in template-based segmentation. This problem will be tackled in future work by formulating the PDE-constrained problem with other image similarity metrics such as Normalized Cross Correlation, local Normalized Cross Correlation, or Mutual Information [31]. We expect that this change in the formulation of the problem will increase the performance results of PDE-constrained LDDMM. In addition, it will allow us to apply these methods to other clinical applications involving multi-modal registration.

Simultaneously to the development of this work, Mang et al. released Claire software [17]. The software is intended to exploit massive CPU based parallel computing architectures to accelerate the computation time of PDE-LDDMM. The codes implement original PDE-constrained LDDMM with a variational extension to nearly incompressible fluids and include H^1 and H^2 regularization terms. The software is restricted to the stationary parameterization of diffeomorphisms. The PDE integration scheme is SL-RK. The software includes a sophisticated multi-level preconditioner that shows to improve the convergence of PCG with respect to the original proposal in [10]. The massive computation allows increasing the number of inner and outer iterations and use the norm of the gradient as stopping condition for achieving an extraordinary accuracy at convergence in a simulated experiment.

In contrast to Claire, our methods of choice are intended to run completely in the VRAM of commodity GPUs ($< 4\text{GBs}$). We have limited the variational formulation to the one proposed in [10], although it is straightforwardly extendible to the nearly incompressible fluid problem. We have limited our study to the traditional LDDMM regularizer. Our software works for the stationary and the non-stationary parameterization of diffeomorphisms. We have limited the preconditioner to the one proposed in [10] since we are interested on the comparison of the three different variational variants. We used the stopping conditions suggested in [31] and used for PDE-LDDMM in [10,12,19,14,16]. The variety of methods, the extensive evaluation conducted in this work, and our modest hardware capacity hindered us the use of the inner and outer iteration values needed for achieving the stopping conditions based on the norm of the gradient suggested in [17]. In fact, we observed in a selected NIREP experiment that increasing the number of inner iterations in PCG resulted into a faster initial convergence that finally stagnated in greater MSE_{rel} values and lower DSC scores than our considered stopping conditions. This stagnation was also reported in [17] for the simulated experiment. Instead, our selected inner and outer values consumed a reasonable amount of time while obtaining state of the art results for the evaluation metrics.

Comparing Claire and our results, we believe that it would be of interest to implement our best performing variant as a part of Claire’s software. In the other direction, it would be very interesting to adopt the multi-level preconditioners in our methods.

7 Conclusions

In this work, we have proposed to combine the two different methodological approaches used to circumventing the huge computational complexity of Gauss–Newton–Krylov PDE-constrained LDDMM. In particular, we have included Semi-Lagrangian Runge-Kutta integration [23] in the variants of band-limited PDE-constrained LDDMM proposed in [19,16] for further increasing the computational efficiency of these methods. The resulting methods have been extensively evaluated in five different datasets following three different evaluation frameworks. To our knowledge, this is the first time that SL-RK integration is implemented in the framework of PDE-LDDMM for the non-stationary parameterization and in the space of band-limited vector fields. Moreover, our work first provides the position achieved by PDE-constrained LDDMM methods in the ranking of Klein et al. evaluation.

This study positions the formulation of BL PDE-constrained LDDMM based on the deformation state equation and SL-RK integration as the best performing among all PDE-constrained LDDMM methods in terms of accuracy and efficiency. The proposed method has reached the highest sensitivity in the classification of stable vs progressive mild cognitive impaired conversors in the Alzheimer’s Disease Neuroimaging Initiative (ADNI) database using convolutional neural networks. This result has been recently published in [27].

In future work, we will extend this formulation to other relevant physically meaningful LDDMM approaches such as the nearly incompressible method in [11], and the geodesic shooting approach in [14]. We will explore the advantages of using the multi-level preconditioner in [17]. We will adapt our methods for the use of alternative image similarity metrics that usually outperform SSD in registration evaluation rankings. Finally, we will work in the understanding of which of the features of PDE-LDDMM allows the exceptional classification rates related with Alzheimer’s disease conversion shown in [27].

Acknowledgements

The author would like to acknowledge the anonymous reviewers for their revision of the manuscript. The author would like to give special thanks to Wen Mei Hwu from the University of Illinois for interesting ideas in the GPU implementation of the methods, and Nacho Navarro and Rosa Badia from the Barcelona Supercomputing Center (BSC) for his help. This work was partially supported by the national research grant TIN2016-80347-R. In addition, this work was supported by NVIDIA through the Polytechnical University of Catalonia / Barcelona Supercomputing Center (UPC/BSC) GPU Center of Excellence.

References

1. Miller, M.I.: Computational anatomy: shape, growth, and atrophy comparison via diffeomorphisms. *Neuroimage* **23** (2004) 19–33
2. Miller, M.I., Qiu, A.: The emerging discipline of computational functional anatomy. *Neuroimage* **45(1)** (2009) 16–39
3. Thompson, D.W.: On growth and form. Cambridge University Press (1917)
4. Younes, L.: Shapes and diffeomorphisms. Springer-Verlag, Berlin, Germany (2010)
5. Sotiras, A., Davatzikos, C., Paragios, N.: Deformable medical image registration: A survey. *IEEE Trans. Med. Imaging* **32(7)** (2013) 1153 – 1190
6. Younes, L.: Jacobi fields in groups of diffeomorphisms and applications. *Q. Appl. Math.* **65** (2007) 113 – 134
7. Hart, G.L., Zach, C., Niethammer, M.: An optimal control approach for deformable registration. *Proc. of the IEEE Conference on Computer Vision and Pattern Recognition (CVPR’09)* (2009)
8. Ashburner, J., Friston, K.J.: Diffeomorphic registration using geodesic shooting and Gauss–Newton optimisation. *Neuroimage* **55(3)** (2011) 954 – 967
9. Vialard, F.X., Risser, L., Rueckert, D., Cotter, C.J.: Diffeomorphic 3D image registration via geodesic shooting using an efficient adjoint calculation. *Int. J. Comput. Vision* **97(2)** (2011) 229 – 241
10. Mang, A., Biros, G.: An inexact Newton-Krylov algorithm for constrained diffeomorphic image registration. *SIAM J. Imaging Sciences* **8(2)** (2015) 1030–1069
11. Mang, A., Biros, G.: Constrained H1 regularization schemes for diffeomorphic image registration. *SIAM J. Imaging Sciences* **9(3)** (2016) 1154–1194
12. Mang, A., Ruthotto, L.: A lagrangian GaussNewtonKrylov solver for mass- and intensity-preserving diffeomorphic image registration. *SIAM J. Sci. Comput.* **39(5)** (2017) B860 – B885

13. Zhang, M., Fletcher, T.: Fast diffeomorphic image registration via Fourier-Approximated Lie algebras. *Int. J. Comput. Vision* (2018)
14. Hernandez, M.: PDE-constrained lddmm via geodesic shooting and inexact Gauss-Newton-Krylov optimization using the incremental adjoint Jacobi equations. *Phys. in Med. and Biol.* **64(2)** (2019)
15. Polzin, T., Niethammer, M., Heinrich, M.P., Handels, H., Modersitzki, J.: Memory efficient LDDMM for lung CT. *Proc. of the 19th International Conference on Medical Image Computing and Computer Assisted Intervention (MICCAI'16)*, Lecture Notes in Computer Science (2014) 28–36
16. Hernandez, M.: A comparative study of different variants of Newton-Krylov PDE-constrained Stokes-LDDMM parameterized in the space of band-limited vector fields. *SIAM J. Imaging Sciences* (2019)
17. Mang, A., Gholami, A., Davatzikos, C., Biros, G.: Claire: A distributed-memory solver for constrained large deformation diffeomorphic image registration. *SIAM J. Sci. Comput.* **41(5)** (2019) C548C584
18. Zhang, M., Fletcher, P.T.: Finite-dimensional Lie algebras for fast diffeomorphic image registration. *Proc. of International Conference on Information Processing and Medical Imaging (IPMI'15)*, Lecture Notes in Computer Science (2015)
19. Hernandez, M.: Band-limited stokes large deformation diffeomorphic metric mapping. *IEEE J. of Biom. and Health Inf.* **23(1)** (2019)
20. Staniforth, A., Cote, J.: Semi-lagrangian integration schemes for atmospheric models - a review. *Mon. Weather Rev.* **119** (1991) 2206 – 2223
21. Beg, M.F., Miller, M.I., Trounev, A., Younes, L.: Computing large deformation metric mappings via geodesic flows of diffeomorphisms. *Int. J. Comput. Vision* **61(2)** (2005) 139–157
22. Guo, D.X.: A Semi-Lagrangian Runge-Kutta method for time-dependent partial differential equations. *Journal of applied analysis and computation* **3(3)** (2013) 251 – 263
23. Mang, A., Biros, G.: A semi-lagrangian two-level preconditioned Newton-Krylov solver for constrained diffeomorphic image registration. *SIAM J. Sci. Comput.* **39(6)** (2017) B1064 – B1101
24. Mang, A., Gholami, A., Biros, G.: Distributed-memory large-deformation diffeomorphic 3D image registration. *Proc. of ACM/IEEE SuperComputing conference (SC16)* (2016)
25. Klein, A., et al.: Evaluation of 14 nonlinear deformation algorithms applied to human brain MRI registration. *Neuroimage* **46(3)** (2009) 786–802
26. Rohlfing, T.: Image similarity and tissue overlaps as surrogates for image registration accuracy: widely used but unreliable. *IEEE Trans. Med. Imaging* **31(2)** (2012) 153 – 163
27. Ramon-Julvez, U., Hernandez, M., Mayordomo, E., ADNI: Analysis of the influence of diffeomorphic normalization in the prediction of stable vs progressive mci conversion with convolutional neural networks. *Proc. of the 17th IEEE International Symposium on Biomedical Imaging: From Nano to Macro (ISBI'20)* (2020)
28. Riishojgaard, L.P., Cohn, S.E., Li, Y., Menard, R.: The use of spline interpolation in semi-lagrangian transport models. *Monthly Weather Review* **126(7)** (1998)
29. Avants, B.B., Epstein, C.L., Grossman, M., Gee, J.C.: Symmetric diffeomorphic image registration with cross-correlation: Evaluating automated labeling of elderly and neurodegenerative brain. *Med. Image Anal.* **12** (2008) 26 – 41
30. Ruijters, D., Thevenaz, P.: GPU prefilter for accurate cubic B-spline interpolation. *The Computer Journal* **55(1)** (2012) 15 – 20

31. Modersitzki, J.: FAIR: Flexible Algorithms for Image Registration. SIAM (2009)

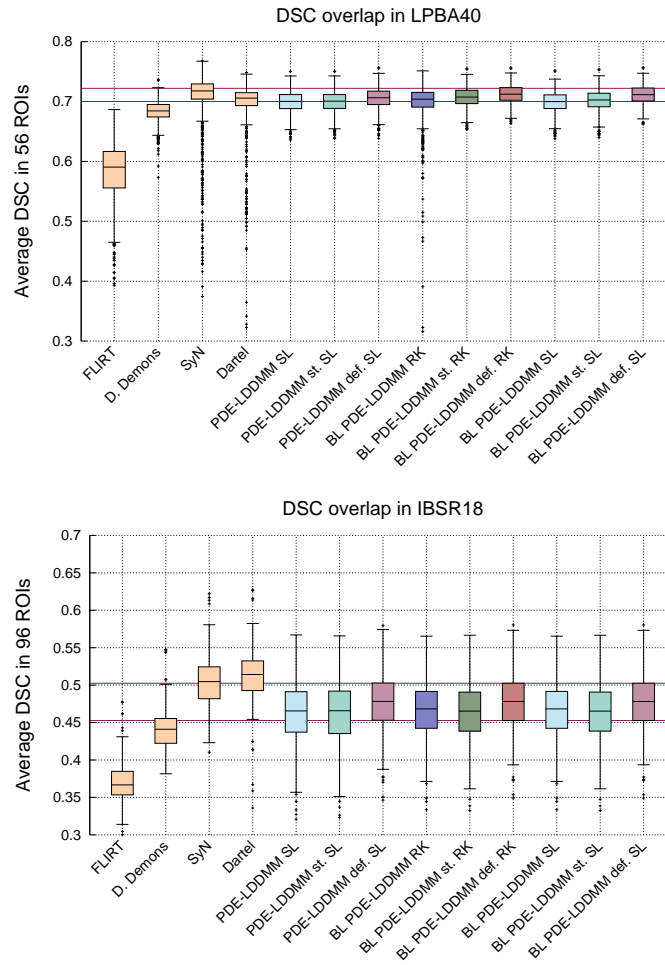


Fig. 3. LPBA40 and IBSR18. Distribution of the DSC values averaged over the manual segmentations in the registration experiments. The whiskers indicate the minimum and maximum of the DSC values. The horizontal red lines indicate the first and third quartiles of BL PDE-LDDMM based on the deformation state equation.

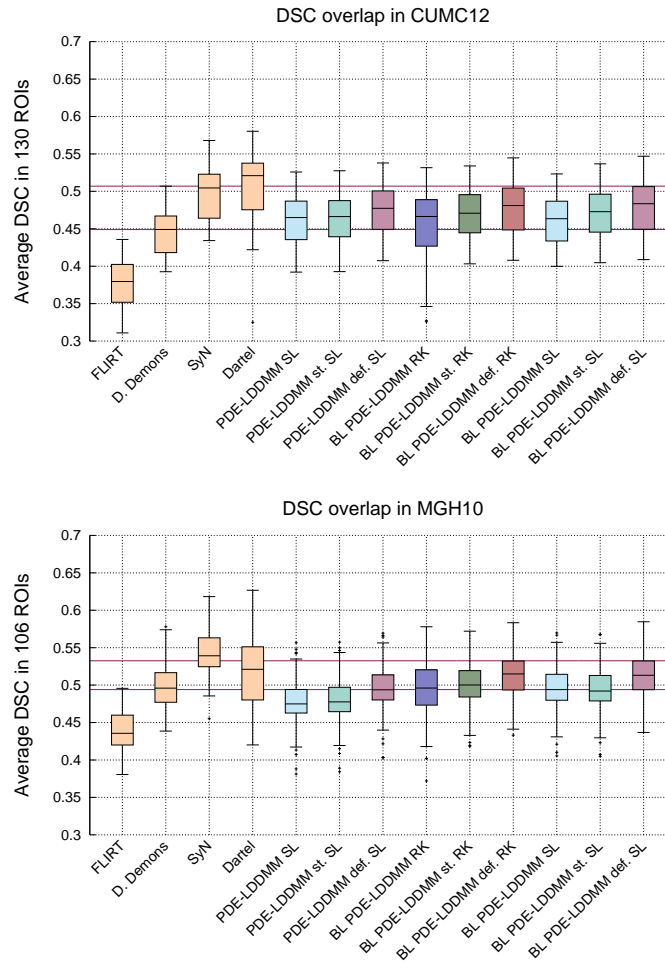


Fig. 4. CUMC12 and MGH10. Distribution of the DSC values averaged over the manual segmentations in the registration experiments. The whiskers indicate the minimum and maximum of the DSC values. The horizontal red lines indicate the first and third quartiles of BL PDE-LDDMM based on the deformation state equation.

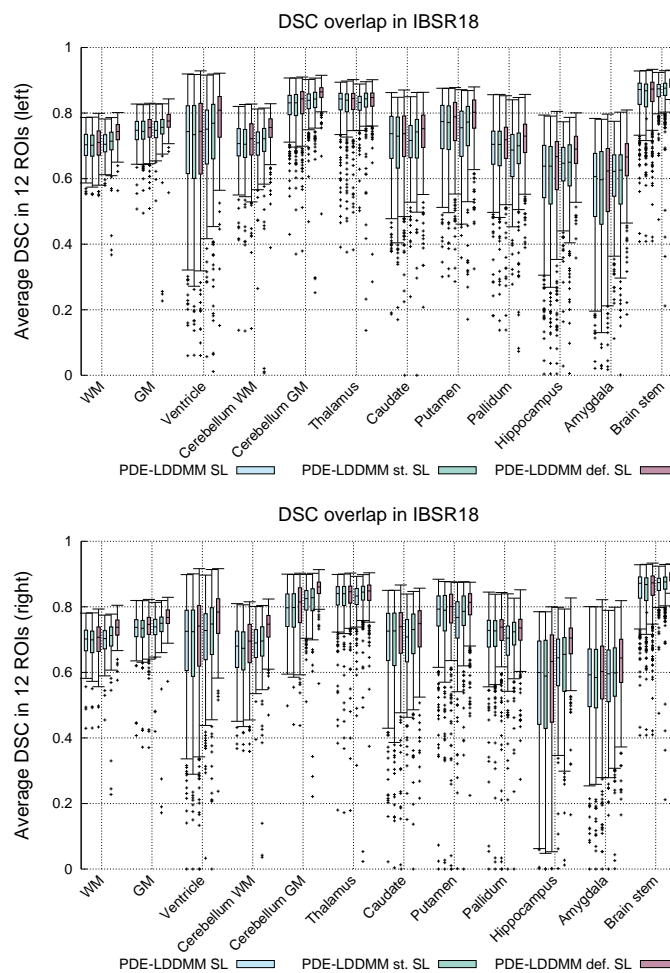


Fig. 5. IBSR18 V2.0. Volume overlap obtained by the proposed registration methods. The box and whisker plots show the distribution of the DSC values averaged over the manual segmentations for each region. The whiskers indicate the minimum and maximum of the DSC values. For each group of plots, the first three correspond with the spatial domain parameterization and the three last with the band-limited domain parameterization. WM and GM stand for white matter and grey matter, respectively.